Importance of non-covalent interactions in a nitrile anion metal-complex based on pyridine ligands: A theoretical and experimental approach

Zouaoui Setifi, Bruno Landeros-Rivera, Peter W.R. Corfield, Diego Gil, Julia Contreras-Garcia, Fatima Setifi, Helen Stoeckli-Evans

ARTICLE

Importance of non-covalent interactions in a nitrile anion metal-complex based on pyridine ligands: a theoretical and experimental approach

Received 00th January 20xx,
Accepted 00th January 20xx

DOI: 10.1039/x0xx00000x

Zouaoui Setifi,[a,b,*] Bruno Landeros-Rivera,[c,*] Peter W. R. Corfield,[d] Diego M. Gil,[e] Julia Contreras-García,[c] Fatima Setifi,[a,*] Helen Stoeckli-Evans[f]

The solvothermal synthesis and crystal structure of [bis(thiocyanato-κ*N*)bis(tris(pyridin-2-yl-κ*N*)amine)iron(II)] (**1**) are described. The obtained structure is then subjected to theoretical analysis of interaction energies and intra- and intermolecular bonding. This comprehensive study allows to illustrate the richness of non-covalent interactions that are exhibited by nitrile anion-metal complexes. The neutral complex lies on a crystallographic two-fold axis. The iron atom is octahedrally coordinated, with two thiocyanato ligands in *cis* positions, and the two trispyridine ligands coordinated via the nitrogen atoms of just two of the three pyridine rings. Energy analysis of five significant dimers, supplemented by a detailed analysis of the Hirshfeld surfaces, indicates attractive interaction energies of up to 101 kJ, with the strongest dimer stabilized by bifurcated C–H···S hydrogen bonds and additional π···π interactions. Theoretical analysis confirms the high-spin nature of the complex which is indicated by the Fe–N bond lengths, and highlights the relevance of intramolecular ligand-ligand interactions. From a combined analysis using the Quantum Theory of Atoms in Molecules and the Non-Covalent Interaction index it was possible to identify further specific intermolecular interactions contributing the stability of the crystal structure, such as the H···H bonds, as well as the presence of several delocalized van der Waals forces, which are mainly of dispersive origin.

Introduction

As a consequence of their ability to link metal ions in a variety of different ways, pseudohalide and polynitrile anions, either functioning alone or in combination with neutral co-ligands, provide opportunities for the generation of molecular architectures with varying dimensions and topologies.[1-8] For instance, due to the nature of their metal-ligand interactions, complex magnetic behaviors can arise in these systems.[9] Furthermore, the chemical richness of the nitrile anionic ligands allows the emergence of other interesting properties. For example, ionic liquids or mixed matrix membranes doped with nitrile anions have shown important capacities for CO_2/N_2 separation[10] or SO_2 capture.[11] These are thought to be the consequence of enhanced specific non-covalent interactions between the anions, which lead to the formation of 3D frameworks that in turn increase the affinity for the guest molecules because of the emergence of stronger intermolecular interactions. Moreover, it is known that the activation of nitriles with a metallic center[12] can increase reactivity by factors[13] that go from 10^3 to 10^{18}. This capacity has been exploited for developing, for example, enantiospecific and enantioselective allylic alkylation reactions whose products can mimic some biological active molecules.[14] Additionally, the use of other nitrogenated neutral co-ligands with relevant catalytic capabilities such as pyridine,[15] could improve the reactive properties of nitrile-transition metal complexes. It has been determined that supramolecular catalysis ultimately depends on the presence of intermolecular interactions (e.g., hydrogen bonds, metal-ligand, and other type of van der Waals forces) among the present species: ligands, metallic centers, catalyst, substrate, additives, etc.[16] This explains the importance of analyzing the vastness of non-covalent interactions that could be formed with polynitrile-metal coordination compounds, which could be exploited for developing materials with new controlled magnetic, capture or catalytic properties.

Crystalline phases are ideal for the analysis of intermolecular interactions in both discrete and infinite-array 3D materials.[17] On the one hand, from good-quality X-ray diffraction experiments the crystal structure of a periodical system can be

[a] *Laboratoire de Chimie, Ingénierie Moléculaire et Nanostructures (LCIMN), Université Ferhat Abbas Sétif 1, Sétif 19000, Algeria.*
[b] *Département de Technologie, Faculté de Technologie, Université 20 Août 1955-Skikda, Skikda 21000, Algeria.*
[c] *Sorbonne Université, CNRS, Laboratoire de Chimie Théorique, LCT, F. 75005 Paris, France.*
[d] *Department of Chemistry, Fordham University, 441 East Fordham Road, Bronx, NY 10458, USA.*
[e] *INBIOFAL (CONICET - UNT), Instituto de Química Orgánica - Cátedra de Química Orgánica I, Facultad de Bioquímica, Química y Farmacia, Universidad Nacional de Tucumán, Ayacucho 471 (T4000INI), San Miguel de Tucumán - Tucumán – Argentina.*
[f] *Institute of Physics, University of Neuchâtel, rue Emile-Argand 11, CH-2000 Neuchâtel, Switzerland.*
† Footnotes relating to the title and/or authors should appear here.
Electronic Supplementary Information (ESI) available: [details of any supplementary information available should be included here]. See DOI: 10.1039/x0xx00000x

obtained, which can be further analyzed by other methods, such as Hirshfeld surface analysis[18] to determine the presence and abundance of different type of interatomic contacts. Also, a study of interaction energies using a partition into different contributions,[19] such as electrostatic, polarization, dispersion or repulsion, can provide additional useful information concerning the driving forces of the crystal stability. On the other hand, some branches of theoretical chemistry like Quantum Chemical Topology can be used to obtain a deeper understanding of the present interactions. From this field, the Quantum Theory of Atoms in Molecules[20] (QTAIM) and the Non-Covalent Interaction index[21] (NCI) stand out and complement each other. The former is optimal for a quantitative characterization of local specific interactions (metal-ligand interactions, hydrogen, halogen or chalcogen bonding, etc.), while the latter allows an easy visualization of regions with delocalized weak interactions (π···π, hydrophobic, etc.).

With this in mind, we have synthethized the novel [bis(thiocyanato-κN)bis(tris(pyridin-2-yl-*κN*)amine)iron(II)] complex (**1**), which is representative of the chemical richness of nitrile anions (in this case, the thiocyanate). Besides, the use of a neutral aromatic heterocyclic, the tris(pyridin-2-yl-*κN*)amine, is expected to supplement the ability of this coordination complex to form stacking interactions. In order to determine the capacity of this prototype compound to form non-covalent interactions, its crystalline structure was determined by a single-crystal X-ray diffraction analysis carried out at ambient conditions. The assessment of the intermolecular interactions stabilizing this system was performed through a Hirshfeld surface analysis and the CE-B3LYP method for evaluating the interaction energies. Besides, further characterization of the non-covalent interactions was carried out by a topological analysis of the DFT-computed electron density, by means of the QTAIM and NCI approaches.

Experimental

General remarks

The starting materials (metal salt and potassium thiocyanate), and used solvents were purchased from commercial sources (analytical reagent grade) and used without further purification. The tris(pyridin-2-yl)amine ligand was synthesized according to the method reported in the literature.[22] The title compound was prepared solvothermally under autogenous pressure.

Physical measurements

Elemental analysis (carbon, hydrogen and nitrogen) was performed using a PerkinElmer 2400 series II CHNS/O analyzer. The solid-state absorption IR spectrum was recorded with a Nicolet 5SX-FTIR spectrometer equipped with a diamond micro-ATR accessory in the 4000–500 cm^{-1} frequency range.

Synthesis

A mixture of $FeSO_4.7H_2O$ (28 mg, 0.1 mmol), tris(pyridin-2-yl)amine (62 mg, 0.2 mmol) and KNCS (16 mg, 0.2 mmol) in H_2O/EtOH (3:1 v/v, 20 mL) was sealed in a Teflon-lined autoclave and heated at 150 °C for 3 days. After cooling to room temperature at a rate of 10 °C h^{-1}, orange-colored crystals of **1** were obtained (yield 42%). Anal. Calcd. (%) for $C_{32}H_{24}FeN_{10}S_2$: C, 57.49; H, 3.62; N, 20.95%. Found: C, 57.21; H, 3.71; N, 21.07%. Main IR band (ATR, cm^{-1}): ν(NCS): 2112(s).

X-ray crystallography

Suitable single crystals of **1** were chosen for an X-ray diffraction study. Crystallographic measurements were collected at 273 K using a Bruker APEXII CCD diffractometer, equipped with a graphite-monochromatized Mo *K*α radiation (λ = 0.71073 Å). Data collections was controlled by the APEX2 software[23] with cell refinement and data reduction performed using SAINT.[23] A multi-scan absorption correction was applied using SADABS.[23] The structure was solved by direct methods using SHELXS–97[24] and refined by full-matrix least squares on F^2 with all data, using SHELXL–2018/3.[24] The hydrogen atoms were constrained to lie at their idealized positions, with C–H bond lengths of 0.93 Å, and temperature factors 20% greater than the U_{eq} of their bonded C atom. Although data were collected out to θ=30.6°, we used only data out to θ=26°, as beyond that angle there were very few reflection intensities above background. Even at θ=26°, less than a third of the intensities had I > 2σ. Full details of the crystal data, data collection and refinement for **1** are summarized in **Table 1**. CCDC 2115084 contains the supplementary crystallographic data for this paper. These data can be obtained free of charge via www.ccdc.cam.ac.uk/data_request/cif, or by emailing data_request@ccdc.cam. ac.uk, or by contacting The Cambridge Crystallographic Data Centre, 12, Union Road, Cambridge CB2 1EZ, UK; fax:+44 1223 336,033.

Theoretical methods

Hirshfeld surface calculations

The Hirshfeld surfaces and their associated two-dimensional (2D) fingerprint plots[25-28] were generated using *CrystalExplorer17.5* software[29] to visualize and quantify the various non-covalent interactions that are responsible of the crystal stabilization. The normalized contact distance (d_{norm}) is a symmetric function of distances to the surface from nuclei inside (*d*i) and outside (*d*e) the Hirshfeld surface, relative to their respective van der Waals (vdW) radii. Graphical plots of the Hirshfeld surfaces mapped with d_{norm} use a red-white-blue color scale, where red indicates shorter contacts, white is used for contacts around the vdW separation, and blue for longer contacts. The 3D d_{norm} surfaces were mapped over a fixed color scale of -0.075 au (red) to +0.50 au (blue). Hirshfeld surfaces of compound **1** were also mapped with the *shape index* and *curvedness* properties.

Interaction energies

The intermolecular interaction energies (E_{tot}) for different structural dimers of **1** were computed by using the *CrystalExplorer17.5* program.[29] The electron density of the molecule for interaction energy calculations has been obtained at B3LYP/6-31G(d,p) level of theory. The interaction energies between molecular pairs are partitioned into coulombic (E_{coul}), polarization (E_{pol}), dispersion (E_{dis}) and exchange-repulsion (E_{rep}) energy contributions, with scale factors of 1.057, 0.740, 0.871 and 0.618, respectively.[19]

Table 1. Crystal data and structure refinement parameters for **1**.

CCDC	2115084
Crystal data	
Chemical formula	$C_{32}H_{24}FeN_{10}S_2$
M_r	668.58
Crystal system, space group	Monoclinic, *P*2/*c*
Temperature (K)	273
a, *b*, *c* (Å)	8.9395 (10), 10.4984 (11), 17.3304 (17)
β (°)	102.571 (3)
V (Å^3)	1587.5 (3)
Z	2
Radiation type	Mo *K*α
□ (mm^{-1})	0.65
Crystal size (mm)	0.22 × 0.15 × 0.09
Data collection	
Diffractometer	Bruker APEXII CCD
Absorption correction	Multi-scan (*SADABS*; Bruker, 2015)
T_{min}, T_{max}	0.789, 0.886
No. of measured, independent and observed [$I > 2\sigma(I)$] reflections	49856, 3108, 2613
R_{int}	0.074
$(\sin\theta/\lambda)_{max}$ (Å^{-1})	0.617
Refinement	
$R[F^2 > 2\sigma(F^2)]$, $wR(F^2)$, S	0.049, 0.119, 1.17
No. of reflections	3108
No. of parameters	204
H-atom treatment	H atom parameters constrained
$\Delta\rho_{max}$, $\Delta\rho_{min}$ (e Å^{-3})	0.42, −0.51

Computational details

Single point solid-state calculations were performed over the experimental crystalline geometry with a PBE0/pob-TZVP-rev2[30] level of theory, with the Crystal 17 software.[31,32] Both the low-spin and high-spin states were considered to determine their relative stability. For the high-spin state, the n_α - n_β electron value was locked to 8 for 30 cycles, using the SPINLOCK keyword. A shrinking factor of 8 was used for both, the Pack-Monkhorst and the Gilat nets. The chosen threshold for the tolerance on change in the total energy was 10^{-7} a.u. The integral tolerances for the bielectronic, coulombic and exchange-repulsion series were 9, 9, 9, 9 and 30, respectively. For the most stable spin-state, the positions of the hydrogen atoms were relaxed by a partial geometry optimization, since the C–H distances are sub estimated by the refinement done with SHELXL.

In order to examine the intra and intermolecular interactions, molecular calculations were carried out on the monomer and the same dimers studied with the *CrystalExplorer17.5* program[19] using the C–H distances obtained from the periodic computation. These were executed with ORCA[33] (version 4.2.0), with the PBE0/def2-TZVP level of theory. A topological analysis of the computed electron density was performed within the Non-Covalent Interaction index (NCI) and the Quantum Theory of Atoms in Molecules (QTAIM) frameworks, using the NCIPLOT4[34] and AIMALL[35] programs, respectively.

Results and discussion

Description of crystal and molecular structure

Compound **1** crystallizes as a neutral Fe(II) molecular complex, $FeL_2(NCS)_2$, L = tris(pyridin-2-yl)amine. The iron (II) atom lies on a crystallographic two-fold axis with two linear thiocyanate ligands coordinated to the iron atom in *cis* positions within a slightly distorted octahedral arrangement around the iron atom. The molecular structure and a packing diagram of **1** are shown in Figures 1 and 2, respectively. The pyridine molecules act as bidentate ligands (with only two out of three ring-nitrogen atoms acting as donors). This completes the six-coordination around the iron atom, with a chelating bond angle at the Fe atom = 83.45(9)° and *trans* bond angles of 170.78(12) and 175.27(11)°. The Fe–$N_{(NCS)}$ bond lengths are each 2.117(3) Å and the two independent Fe–N distances to the ligands are 2.195(2) and 2.216(3) Å, with the bond *trans* to the thiocyanate ligand being slightly longer. Both types of Fe–N bond length are consistent with a high-spin state for the Fe atom, as Fe–N bond lengths are typically shorter for low-spin complexes. In a recent study of the structure of the low-spin salt $FeL_3(ClO_4)2$,[36] the Fe–N bond lengths averaged 1.98 Å, and in a similar Fe(II) thiocyanate crystal structure which contained both high-spin and low-spin molecules,[37] average Fe–$N_{(pyr)}$ bond lengths were reported as 1.96 Å for the low-spin complex and 2.13 Å for the high-spin complex, with corresponding Fe–$N_{(NCS)}$ bond lengths of 1.94 and 2.15 Å. Additionally, from the periodic DFT computations carried out over the experimental geometry, it was determined that the high-spin state is more stable by 28.6 kcal/mol. According to the Mulliken population analysis, 3.8 unpaired electrons are located in the Fe(II) metallic centre, which agrees with common expectation.

The central amine nitrogen atom in the ligand (N1) shows a trigonal planar geometry, with bond lengths ranging from 1.408(4) to 1.426(4) Å and angles within 1.5° away from 120°. This N atom and its coordinated C atoms are co-planar, with mean deviation from planarity of 0.01 Å. The uncoordinated pyridine ring is twisted only 5.6(1)° from this plane, while the two rings that are coordinated to the Fe atom are twisted by 64.8(1) and 54.7(1)°. Out of 66 structures in the Cambridge Structural Database (CSD, V5.42, last update February 2021; Groom et al., 2016) that involve a transition metal centre coordinated by this ligand, 18 involve the ligand coordinated in

a bidentate manner as in the present structure, and in all them except for one the central N atom has a geometry close to a trigonal planar, and the uncoordinated ligand has only a small torsional angle with the central NC_3 plane. In contrast, in 12 structures where the ligand is tridentate, the central N atom adopts a flattened tetrahedral geometry, as in reference.[36]

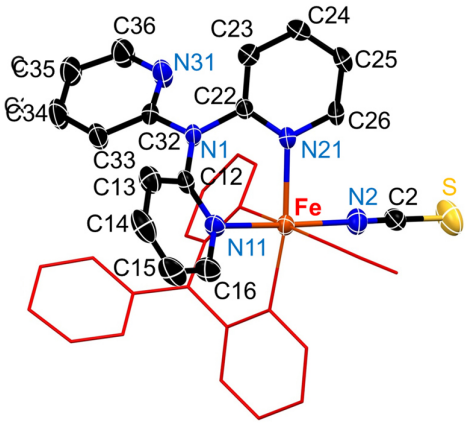

Figure 1. A view of the molecular structure of **1** showing the labels of the non-H atoms, with thermal ellipsoids shown with 50% probability for the asymmetric unit, and the symmetry-related part of the molecule shown in line form. H-atoms were omitted for clarity.

The molecules are linked into chains along the ***a*** direction by C–H···N hydrogen bonds, and the chains are linked into sheets in the ***ac*** plane by weak π-bonding interactions between the pyridine rings and by weak C–H···S hydrogen bonds, which also link the sheets into a three-dimensional network. The only hydrogen bonds are C15–H15···N31(1-x,y,z), with H···N = 2.58 Å, C–H···N angle of 134˚ and C···N distance of 3.291(4) Å. These hydrogen bonds are shown as dashed red lines in Figure 2. π-stacking interactions occur between the pyridine ring (N21/C22-C26) and its neighbour related by the centre of symmetry at (1/2,1/2,1/2). The perpendicular distance between these parallel rings is 3.826(4) Å and there are five separate N/C···C interactions with distances ranging from 3.89 to 3.95 Å. These rings are labelled in red as R1 in the packing diagram (Figure 2). The linear Fe–NCS arms project out into a hydrophobic environment stabilized by weak C–H···S interactions, which link any given molecule to other molecules in all three directions in space. Details of some of these interactions are given in Table 2, and the four shortest ones are shown as dashed green lines in the packing diagram (Figure 2). Upon analysis of the CSD for C–H···SCN-Fe interactions measuring less than the sum of the van der Waal's radii, we found eight entries, whose H···S distances range from 2.73 to 2.95 Å. Although the H···S distances of 2.99 to 3.29 Å in the present structure imply rather weak interactions, the number of these interactions may make them significant in the intermolecular forces holding the crystal structure in place.

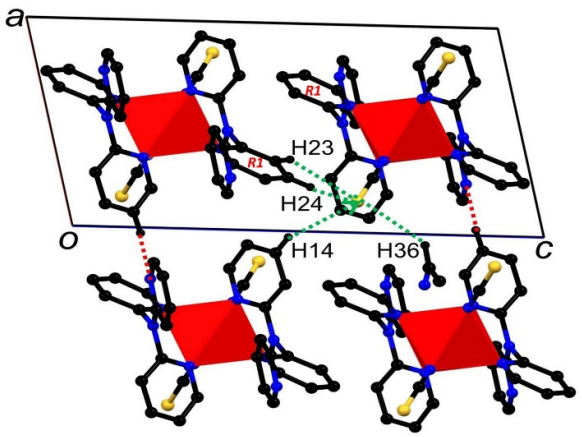

Figure 2. Packing diagram, with view tilted 10° from the **b** axis. The reference molecule is at the right of the unit cell outline; the other molecule is related by the glide plane. C–H···N hydrogen bonds are shown as dashed red lines, while C–H···S contacts less than 3.25 Å are shown as dashed green lines. The link to H36 is to a pyridine ring one unit cell up the b axis, in the direction of the viewer. Only part of that pyridine ring is shown. Pyridine rings labelled R1 in red are expected to be linked by π interactions.

Table2. Geometrical parameters for C–H···S contacts observed in the crystal structure of 1. All distances are in Å and the angle in degrees.

Contact[a]	d(C–H)	d(H···S)	Angle C–H···S	d (C···S)
C14-H14···S(x-1,1-y,z-½)	0.93	2.99	135	3.71
C36-H36···S(2-x,y-1,1½ -z)	0.93	3.15	130	3.81
C23-H23···S(x,1-y,z-½)	0.93	3.16	129	3.81
C24-H24···S(x,1-y,z-½)	0.93	3.25	124	3.85
C33-H33···S(1-x,y-1,1½ -z)	0.93	3.28	135	4.00
C35-H35···S(2-x,y-1,1½ -z)	0.93	3.29	122	3.87

[a]Contacts where both C···S and H···S distances are less than the sum of the van der Waal's Radii +0.5 Å are tabulated.

Energy framework analysis on interaction energies

The intermolecular interaction energies were calculated to identify energetically significant dimers from the crystal structure of **1**. The complete information, including interaction geometries and the different energy components of total intermolecular interactions for dimers are given in Table 3. The main structural motifs that are responsible of the crystal packing of the complex are shown in Figure 3.

The energetic calculations revealed that there are five energetically significant structural motifs (D1-D5) identified from the crystal structure. The total intermolecular interaction energies (E_{tot}) are in the range from -101.9 to -19.1 KJ/mol (see Figure 3, Table 3). The highest total energy of -101.9 KJ/mol corresponds to a molecular pair formed by the bifurcated C24–

H24···S and C23–H23···S hydrogen bonds (Dimer 1, Figure 3). In addition, this structural dimer is also stabilized by C24–H24···C2 and π···π stacking interactions between the centroids of the N21/C22–26 rings [Cg···Cg inter-centroid distance of 3.92 Å]. The electrostatic and dispersion energies contribute 52.5 and 47.5 %, respectively towards stabilization of dimer D1. Dimer 2 is formed by an intermolecular C33–H33···S hydrogen bond involving the sulfur atom of the thiocyanate group and the H33 atom. The electrostatic and dispersion energies contribute 52.1 and 47.9 %, respectively towards the stabilization of this dimer. The dimer D3 (E_{tot} = -54.4 KJ/mol) is mainly stabilized by intermolecular C14–H14···S hydrogen bonds. This interaction is the strongest of all the H···S hydrogen bonds in the crystal packing of **1** as expected from its geometrical parameters reported in Table 1. Further, the intermolecular C15–H15···N31 hydrogen bond stabilizes the dimer D4 (E_{tot} = -44.8 KJ/mol). It should be noted that the electrostatic energy contributes about 82.1 % towards the stabilization of dimer D3. In contrast, dimer D4 is predominantly dispersive in nature (dispersion represents 74.8 % of the stabilization energy). Finally, dimer D5 is stabilized by two C–H···S hydrogen bonds involving the sulfur atom of the thiocyanate moiety and the H35 and H35 atoms from the pyridine ring. The electrostatic and dispersion energies contribute 73 and 27 %, respectively towards the stabilization of this dimer.

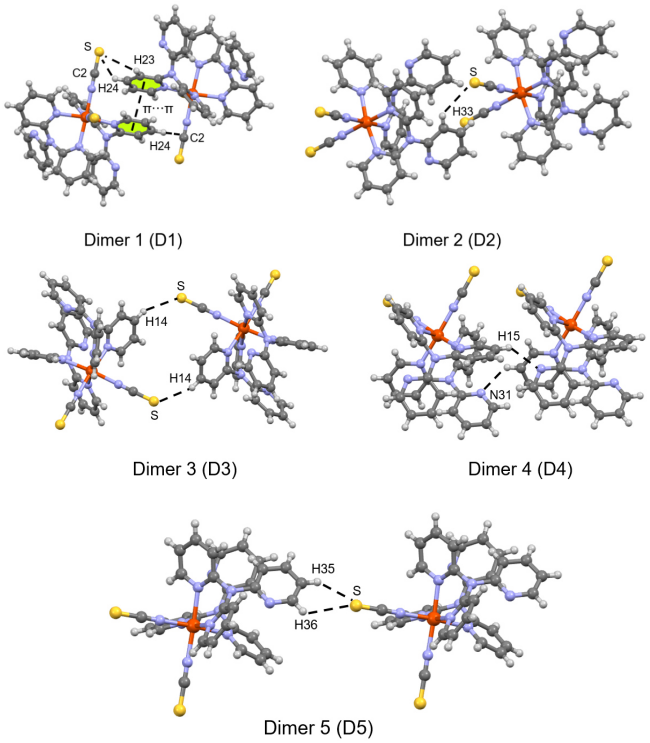

Figure 3. Structural motifs observed in the crystal structure of **1**.

Hirshfeld surface analysis

To explore and quantify the intermolecular interactions in complex 1, the Hirshfeld surfaces and their associated two-dimensional fingerprint (FP) plots were generated. The Hirshfeld surfaces mapped over d_{norm} property are shown in Figure 4, highlighting the main intermolecular contacts and scheme of labels. The full FP plot and those delineated into H···C/C···H and H···S/S···H contacts are depicted in Figure 5, showing the relative percentage contribution to the Hirshfeld surface.

The H···H contacts represent the largest contribution (38%) to the Hirshfeld surface, and they are highlighted in the middle of scattered points in the FP with a minimum value of $(d_e + d_i) \approx$ 2.2 Å, which is near to the sum of vdW radii. The two large bright-red spots labeled 1 on the d_{norm} surface show H···N/N···H contacts associated to C15-H15···N31 hydrogen bonds. These interactions are also visible in the FP plot as symmetrical spikes centered at $(d_e + d_i) \approx$ 2.4 Å, with 7.3% contribution to the Hirshfeld surface area.

The red regions labeled 2 in the Hirshfeld surface mapped over d_{norm} function indicate H···C/C···H contacts attributed to C24–H24···C2 interactions involving the C2 atom of the thiocyanate moiety. These H···C/C···H contacts are also visible in the FP plots as sharp spikes at $(d_e + d_i) \approx$ 2.7 Å, contributing 27.3 % to the total Hishfeld surface area. In addition, the existence of C24–H24···C2 interactions can be seen on the Hirshfeld surface mapped over shape index property, showing surface patches with a large red depression above the C2 atom of the thiocyanate group, and a blue region surrounding the C24–H24 donor (see Figure 4).

Table 3. Intermolecular interaction energies (E_{tot}) partitioned into coulombic (E_{coul}), polarization (E_{pol}), dispersion (E_{dis}) and exchange-repulsion (E_{rep}) contributions (in KJ/mol) for different molecular pairs in **1**.

Dimer	R	Symmetry code	Involved interactions	Geometry (Å, º)	E_{coul}	E_{pol}	E_{dis}	E_{rep}	E_{tot}
D1	9.23	-x, -y, -x	C24–H24···C2	2.79, 133	-54.7	-17.9	-60.0	30.8	-101.9
			C24–H24···S	3.25, 124					
			C23–H23···S	3.16, 129					
			Cg···Cg	3.92					
D2	10.50	x, y, z	C33–H33···S	3.29, 135	-45.2	-18.3	-54.2	32.2	-85.5
D3	11.46	-x, -y, -x	C14–H14···S	2.99, 135	-47.1	-7.99	-10.5	11.2	-54.4
D4	8.94	x, y, z	C15–H15···N31	2.58, 134	-6.76	-11.5	-56.5	30.0	-44.8
D5	13.79	x, y, z	C35–H35···S	3.28, 122	-13.8	-3.99	-6.01	4.82	-19.1
			C36–H36···S	3.15, 130					

ARTICLE

The occurrence of small white spots (labeled 3) on the d_{norm} surface showing H···S/S···H contacts are associated to C14–H14···S hydrogen bonds (see Figure 4). These contacts can also be observed as a pair of sharp symmetrical spikes at (d_e + d_i) ≈ 2.9 Å with a high contribution of 23.2 % to the overall Hirshfeld surface area. As was mentioned previously, the crystal packing of **1** is also stabilized by weak π···π stacking interactions. They occur between layers of pyridine rings. C···C contacts appear as a characteristic pale blue to green area highlighted in red in the full FP plot (Figure 5) at around d_e = d_i = 1.8 Å, with a contribution of 2.9 %. We have performed a close examination of shape index and curvedness surfaces to identify π···π stacking interactions. The pattern of touching red and blue triangles on the shape index (marked with red arrows in Figure 4, at left) is characteristic of π···π stacking interactions. In addition, this type of interaction is also visible in the curvedness Hirshfeld surface as relatively large and green flat regions delineated by red circles.

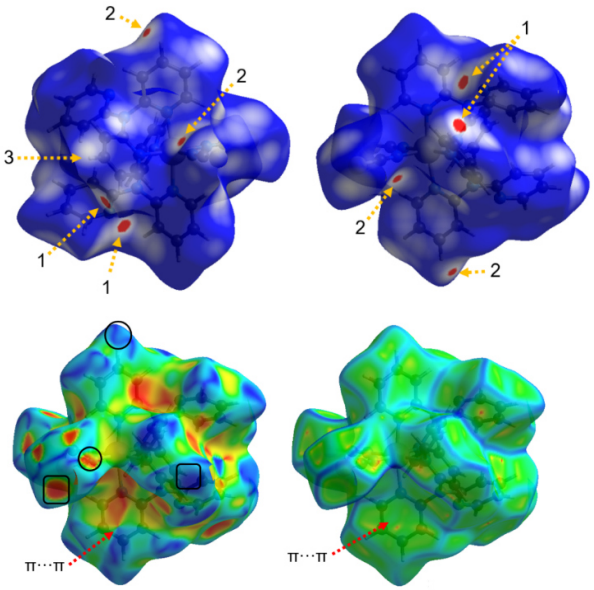

Figure 5. Hirshfeld surfaces of **1** mapped over d_{norm} (in two orientations; the second molecule is rotated 180º around the horizontal axis of the plot), *shape index* and *curvedness* properties.

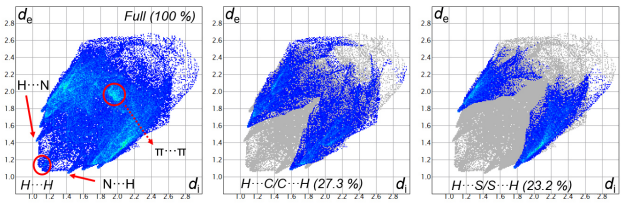

Figure 4. Full and decomposed 2D fingerprint plots for **1**.

Topological analysis

The NCI index[21] provides an intuitive way to visualize the presence of non-covalent interactions by the analysis of 3D isosurfaces. The NCI isosurfaces of the monomer is depicted in Figure 6. Six blue well-defined disks are found around the Fe atom, which correspond to the N→Fe dative bonds. The shape and color of the disks indicates that these are very strong localized interactions. More quantitative information is obtained from the QTAIM analysis.[20] The presence of a bond critical point (BCP), which correspond to special points of the 3D space where the gradient of the electron density vanishes, and a corresponding bond path (gradient lines that connect two bonded nuclei), indicate the existence of some type of bonding which can be covalent or non-covalent. The presence of the N→Fe bonds is corroborated by the finding of six BCP around the iron center. The value of the electron density at the BCP, ρ_B, is proportional to the interaction strength for a given family. Also, the sign of the Laplacian of the electron density at the BCP, $\nabla^2\rho_B$, indicates if the interaction is covalent (negative) or non-covalent (positive). The values of ρ_B for the N2→Fe, N21→Fe and N31→Fe dative bonds are 0.0660, 0.0577 and 0.0552 a.u., respectively, which indicates that the interaction with the NCS ligand is slightly stronger. The values of $\nabla^2\rho_B$ are positive in all cases, confirming the non-covalent nature of the N→Fe dative bonds.

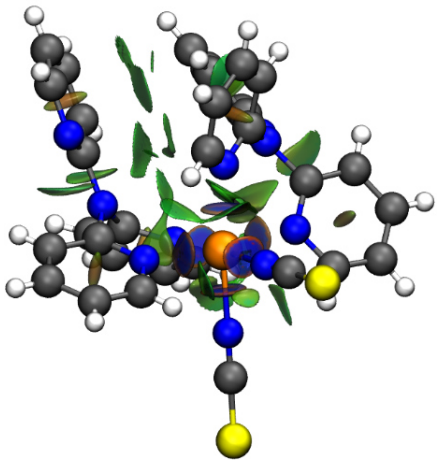

Figure 6. NCI isosurface (0.5) of **1**, obtained from the DFT molecular calculation.

Additionally, the delocalization index defined within QTAIM allows to quantify the amounts of electrons shared between two atoms,[38] or between two group of atoms (calculated as the sum of the delocalization indexes calculated between all the pairs formed from atoms belonging to different groups). The electrons shared between each of the NCS and the tris(pyridin-2-yl)amine ligands with the Fe(II) center are 0.41 and 0.74, respectively. This result indicates that there exist also interactions among the ligands, which can be observed from the green flat extended surfaces found in the rest of the molecule (Figure 6). These types of surfaces are typical of delocalized weak interactions, which in this correspond to van der Waals forces exerted between the ligands.

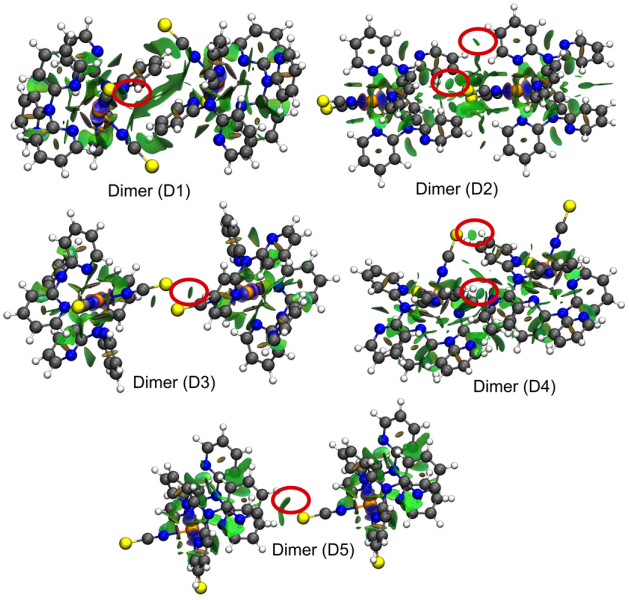

Figure 7. NCI isosurfaces (0.5) of dimers D1-D5. Some relevant localized interactions are circled in red.

The values of ρ_B and $\nabla^2\rho_B$, as well as the interatomic distance of all intermolecular BCPs corresponding to intermolecular interactions are depicted in Table 4. Note that all interactions have positive $\nabla^2\rho_B$, and ρ_B values that are at least one order of magnitude smaller than those of the N→Fe dative bonds, except for the C-H···N found in Dimer D4, which is the strongest intermolecular interaction. Most of the remaining interatomic contacts have been already described in Tables 2 and 3. The exception are the so-called hydrogen–hydrogen bonds,[39] H···H, which have been shown to be important for the stability of some crystalline systems.[40] A possible reason is that the H···H distances were underestimated during the crystallographic refinement. The C–H distances obtained from the partial geometry optimization are in the interval 1.08–1.09 Å, which are about 0.15 Å larger than those obtained with SHELXL. In Dimer D2 the strongest interaction is a hydrogen–hydrogen bond formed between H26 and H34, which shows the shortest interatomic distance (2.41 Å). There is also a S···S interaction that was found at a large distance (5.74 Å), which is nevertheless the weakest of all.

A complementary analysis of the non-covalent interactions is provided by the NCI method. Some of the most relevant localized interactions are marked by red circles in Figure 7. Just like the N→Fe bonds, these have a definite disk shape. However, they show a green color, which corroborates that they are weaker, in agreement with the QTAIM analysis. Moreover, most of the BCPs are embedded in the green extended surfaces, which are abundant in dimers D1, D2 and D4. Thus, these three dimers are stabilized mainly by van der Waals dispersive interactions, which agrees with the fact that the dispersion interaction is dominant for these systems (Table 3). In contrast, dimers D3 and D5 are stabilized mostly by localized C-H···S hydrogen bonds, which explains why the electrostatic interaction is larger for these two dimers (Table 3).

Conclusions

A novel compound, **1**, was synthetized and taken as prototype for the analysis of the supramolecular chemistry of nitrile anion-metal complexes. The combination of X-ray structure results and detailed theoretical analysis presented here reflects increasing interest in such analysis in structural chemistry, which can lead to deeper understanding of molecular bonding and of interactions in crystals. Quantitative discussion of non-covalent interactions is key to understanding structure and function in biomolecules as well as the solid-state chemistry of organic and inorganic compounds. The variety of computational tools used in this work provides complementary perspectives on the quantitative study of the intermolecular interactions. For instance, from a geometrical analysis of N→Fe distances and solid-state DFT calculations it was determined that this compound has a high-spin state. The theoretical analysis of energetically significant dimer configurations identifies specific key C–H···S attractive interactions which can be correlated with C···S distances from the X-ray determination, while the one C–

H···N intermolecular interaction found in the theoretical studies correlates with the C–H···N hydrogen bond found in the X-ray structure, and evidence for both of these interactions is indicated by the Hirshfeld fingerprint plots. Furthermore, the analysis by means of QTAIM provided a quantitative characterization of all types of non-covalent interactions, from N→Fe dative bonds, to weak S···S chalcogen bonds. Moreover, from this analysis it was possible to locate the presence of non-classical interactions such as the H···H bonds, which are not easily found by the crystallographic analysis. Finally, from the detection of regions or localized and delocalized interactions, it was possible to explain why some dimers are dominated by dispersion effects while the coulombic contribution is more important in others.

Table 4. Values of the interatomic distances, ρ_B and $\nabla^2\rho_B$ for each of the intermolecular BCPs found for dimers D1–D5 of **1**.

Interaction	Distance (Å)	ρ_B (a.u)	$\nabla^2\rho_B$ (a.u)
D1			
C2···H24	2.79	0.0068	0.0237
S···H23	3.16	0.0061	0.0181
C13···H25	2.91	0.0060	0.0181
C23···C25	3.90	0.0026	0.0081
D2			
H26···H34	2.41	0.0062	0.0217
H26···H35	2.42	0.0057	0.0210
N2···H34	3.13	0.0050	0.0170
S···H33	3.29	0.0048	0.0136
S···C35	3.75	0.0046	0.0140
N2···H34	3.02	0.0040	0.0146
D3			
S H14	2.99	0.0076	0.0227
D4			
N31···H15	2.58	0.0113	0.0369
C14···H36	2.96	0.0058	0.0199
C23···H15	3.01	0.0052	0.0170
S···H25	3.51	0.0033	0.0086
H36···H36	3.20	0.0022	0.0081
H15···H16	3.09	0.0016	0.0063
S···S	5.74	0.0003	0.0007
D5			
S···H35	3.29	0.0047	0.0139
S···H36	3.15	0.0048	0.0156

Conflicts of interest

There are no conflicts to declare.

Acknowledgements

We are grateful to the Algerian Ministère de l'Enseignement Supérieur et de la Recherche Scientifique (MESRS), the Direction Générale de la Recherche Scientifique et du Développement Technologique (DGRSDT) as well as the Université Ferhat Abbas Sétif 1 for financial support. B. L-R. thanks to CONACyT for the posdoctoral fellowship (CVU 366057).

Notes and references

1 Z. Setifi, M. Ghazzali, C. Glidewell, O. Perez, F. Setifi, C. J. Gomez-Garcia and J. Reedijk, *Polyhedron*, 2016, **117**, 244-248.
2 Z. Setifi, F. Setifi, C. Glidewell, D. M. Gil, A.V. Kletskov, J. Echeverria and M. Mirzaei, *J. Mol. Struct*., 2021, **1235**, 130155.
3 F. Setifi, J. M. Knaust, Z. Setifi and R. Touzani, *Acta Crystallogr., Sect. E: Crystallogr. Commun*., 2016, **72**, 470-476.
4 C. Krebs, M. Ceglarska, and C. Näther, *Z. Anorg. Allg. Chem*., 2021, **647**, 552-559.
5 A. Addala, F. Setifi, K. G. Kottrup, C. Glidewell, Z. Setifi, G. Smith and J. Reedijk, *Polyhedron*, 2015, **87**, 307-310.
6 S. Benmansour, F. Setifi, S. Triki, J. Salaün, F. Vandevelde, J. Sala-Pala, C. J. Gómez-García and T. Roisnel, *Eur. J. Inorg. Chem.*, 2007, 186–194.
7 S. Benmansour, F. Setifi, S. Triki, and C. J. Gómez-García, *Inorg. Chem.*, 2012, **51**, 2359–2365.
8 A. O. Dmitrienko, M.l I. Buzin, Z. Setifi, F. Setifi, E. V. Alexandrov, E. D. Voronova and A. V. Vologzhanina, *Dalton Trans*., 2020,**49**, 7084-7092.
9 S. Benmansour, C. Atmani, F. Setifi, S. Triki, M. Marchivie and C. J. Gómez-García, Polyhedron, 2010, 254, 1468-1478.
10 H. Zhao, L. Feng, X. Ding, Y. Zhao, X. Tan and Y. Zhang, *J. Membr. Sci.*, 2018, **564**, 800-805.
11 C. Wang, J. Zheng, G. Cui, X. Luo, Y. Guo and H. Li, *Chem. Commun.*, 2013, **49**, 1166-1168.
12 N. A. Bokach, *Russ. J. Coord. Chem*., 2018, **44**, 227–242.
13 A. S. Kritchenkov, N. A. Bokach, G. L. Starova and V. Y. Kukushkin*, Inorg. Chem*., 2012, **51**, 11971–11979.
14 M.Tom and P. A. Evans, *Synlett*, 2021, DOI: 10.1055/a-1696-5713.
15 X. Zhang, Y. B. Mollamahale, D. Lyu, L Liang, F. Yu, M.Qing, Y. Du, X. Zhang, Z. Qun Tian and P.K. Shen, *J. Catal*., 2019, **372**, 245-257.
16 M. Raynal, P. Ballester, A. Vidal-Ferrana and P. W. N. M. van Leeuwen, *Chem. Soc. Rev.*, 2014, **43**, 1660-1733.
17 A. K. Nangia and G. R. Desiraju, *Angew. Chem. Int. Ed*., 2019, **58**, 4100-4107.
18 M. A. Spackman and D. Jayatilaka, *CrystEngComm*, 2009, **11**, 19-32.
19 C. F. Mackenzie, P. R. Spackman, D. Jayatilaka and M. A. Spackman, *IUCrJ*, 2017, **4**, 575-587.
20 R. F. W. Bader and T. T. Nguyen-Dang, *Adv. Quantum Chem*., 1981, **14**, 63-124.
21 E. R. Johnson, S. Keinan, P. Mori-Sánchez, J. Contreras-García, A. J. Cohen and W. Yang, *J. Am. Chem. Soc*., 2010, **132**, 6498–6506.
22 W. Yang, H. Schmider, Q. Wu, Y. Zhang and S. Wang*, Inorg. Chem*., 2000, **39**, 2397–2404.
23 Bruker, APEX2, SAINT and SADABS, Bruker AXS Inc., Madison, Wisconsin, USA, 2015.
24 G. M. Sheldrick, *Acta Crystallogr., Sect. A: Found. Adv*., 2015, **71**, 3-8.
25 J. J. McKinnon, M. A. Spackman and A. S. Mitchel, *Acta Crystallogr., Sect. B: Struct. Sci., Cryst. Eng. Mater*., 2004, **60**, 627-668.
26 Y. H. Luo, C. Chen, D. L. Hong, X. T. He, J. W. Wang and B. W. Sun*, J. Phys. Chem. Lett*., 2018, **9**, 2158-2163.
27 J. J. McKinnon, D. Jayatilaka and M. A. Spackman*, Chem. Commun*., 2007, 3814-3816.
28 M. A. Spackman, Chem. Rev., 1992, **92**, 1769-1797.
29 M. J. Turner, J. J. McKinnon, S. K. Wolf, D.J. Grimwood, P. R. Spackman, D. Jayatilaka, M. A. Spackman, CrystalExplorer17, 2017. University of Western Australia: Perth.

30 D. V. Oliveira, J. Laun, M. F. Peintinger and T. Bredow, *J. Comput. Chem.*, 2019, **40**, 2364-2376.
31 R. Dovesi, A. Erba, R. Orlando, C. M. Zicovich-Wilson, B. Civalleri, L. Maschio, M. Rerat, S. Casassa, J. Baima, S. Salustro and B. Kirtman, *WIREs Comput. Mol. Sci*., 2018, **8**, e1360.
32 R. Dovesi, V. R. Saunders, C. Roetti, R. Orlando, C. M. Zicovich-Wilson, F. Pascale, B. Civalleri, K. Doll, N. M. Harrison, I. J. Bush, P. D'Arco, M. Llunell, M. Causà, Y. Noël, L. Maschio, A. Erba, M. Rerat and S. Casassa, CRYSTAL17 User's Manual (University of Torino, Torino, 2017).
33 F. Neese, F. Wennmohs, U. Becker and C. Riplinger, *J. Chem. Phys*., 2020, **152**, 224108.
34 R. A. Boto, F. Peccati, R. Laplaza, C. Quan, A. Carbone, J. P. Piquemal, Y. Maday and J. Contreras-García*, J. Chem. Theory Comput.,* 2020, **16**, 4150-4158.
35 AIMAll (Version 16.10.09), Todd A. Keith, TK Gristmill Software, Overland Park KS, USA, 2016 (aim.tkgristmill.com).
36 Z. Setifi, F. Setifi, N. Dege, R. El Ati and C. Glidewell, *Acta Crystallogr., Sect. E: Crystallogr. Commun*., 2018, **74**, 668-672.
37 S. Bonnet, M. A. Siegler, J. Sánchez Costa, G. Molnár, A. Bousseksou, A. L. Spek, P. Gamez and J. Reedijk, *Chem. Commun.*, 2008, 5619-5621.
38 C. L. Firme, O. A. C. Antunes and P. M. Esteves*, Chem. Phys. Lett.,* 2009, **468**, 129-133.
39 C. F. Matta, J. Hernández-Trujillo, T. Tang and R. F. W. Bader, *Chem. Eur. J.*, 2003, **9**, 1940-1951.
40 J. C. García-Ramos, F. Cortés-Guzmán and C. F. Matta, in *Intermolecular Interactions in Crystals: Fundamentals of Crystal Engineering*, ed. J. J. Novoa, Royal Society of Chemistry, London, UK, 2018, ch. 16, pp. 559-594.